AGU PUBLICATIONS

JGR

Journal of Geophysical Research: Oceans

RESEARCH ARTICLE

10.1002/2016JC011638

Special Section:
Forum for Arctic Modeling and Observational Synthesis (FAMOS): Results and Synthesis of Coordinated Experiments

A dynamical model of Kara Sea land-fast ice

Einar Olason[1,2]

[1]Max Planck Institute for Meteorology, Hamburg, Germany, [2]Nansen Environmental and Remote Sensing Center, Bergen, Norway

Abstract This paper introduces modifications to the traditional viscous-plastic sea-ice dynamical model, which are necessary to model land-fast ice in the Kara Sea in a realistic manner. The most important modifications are an increase in the maximum viscosity from the standard value of $\zeta_{max}=(2.5\times10^8\text{s})P$ to $\zeta_{max}=(10^{13}\text{s})P$, and to use a solver for the momentum equation capable of correctly solving for small ice velocities (the limit here is set to 10^{-4} m/s). Given these modifications, a necessary condition for a realistic fast-ice simulation is that the yield curve give sufficient uniaxial compressive strength. This is consistent with the idea that land-fast ice in the Kara Sea forms primarily via static arching. The modified model is tested and tuned using forcing data and observations from 1997 and 1998. The results show that it is possible to model land-fast ice using this model with the modifications mentioned above. The model performs well in terms of modeled fast-ice extent, but suffers from unrealistic break-ups during the start and end of the fast-ice season. The main results are that fast ice in the Kara Sea is supported by arching of the ice, the arches footers resting on a chain of islands off shore.

Key Points:
- Fast ice in the Kara Sea is held in place by static arching of the ice between islands
- Internal model dynamics determine the fast-ice extent, formation, and break-up for the first time
- Correct uniaxial compressive strength and high maximum viscosity is necessary to simulate fast ice

Correspondence to:
E. Olason,
einar.olason@nersc.no

Citation:
Olason, E. (2016), A dynamical model of Kara Sea land-fast ice, *J. Geophys. Res. Oceans*, *121*, 3141–3158, doi:10.1002/2016JC011638.

Received 11 JAN 2016
Accepted 12 APR 2016
Accepted article online 15 APR 2016
Published online 13 MAY 2016

1. Introduction

Land-fast ice can be found all around the Arctic rim, but it is an especially prominent feature of the Siberian winter ice cover, with the Kara, Laptev and East-Siberian Seas all having extensive fast-ice cover in winter. Of these, the Kara Sea fast-ice cover is probably the most observed and studied (see in particular *Divine et al*. [2003, 2004, 2005]). Fast ice in the Kara Sea has historically closed the Vilkitsky Strait, separating the Laptev and Kara Seas, for about 7 months of the year. The presence of ice there is arguably the most difficult road block for the North-East passage. Fast ice has, in general considerable effects on navigation. Land-fast ice also has a considerable effect on the ocean and atmosphere at a regional scale. With ever increasing computing powers these effects may soon be of interest to researchers running basin-scale or even global models.

Despite its importance, the dynamical modeling of land-fast ice has not garnered much interest in the sea-ice modeling community. Most dynamic sea-ice models are not able to reproduce land-fast ice in a realistic setting, based on the ice dynamics. *Zyryanov and Korsnes* [2003] did simulate fast-ice formation in the Kara Sea under idealized wind stress using a cohesive discrete element model. This model shares some very basic rheological characteristics with the model proposed here, but they use a discrete element model is substantially different from the continuous finite-difference model used here. *Dumont et al*. [2009] used an elasto-viscous-plastic model to simulate the North Water Polynya ice bridge using idealized forcing and decreased ellipse aspect ratio. *König Beatty and Holland* [2010] introduced tensile strength to the elliptic yield curve of the viscous-plastic and elasto-viscous-plastic models in order to model fast ice, but only considered idealized one dimensional cases. Parametrizations of fast-ice formation due to the grounding of pressure ridges have been introduced into classical sea-ice models [*Lieser*, 2004; *Lemieux et al*., 2015], covering fast ice formation over shallow waters, through the mechanism of ice anchoring. In a pan-Arctic simulation, *Itkin et al*. [2015] used the modifications of *König Beatty and Holland* [2010] to model fast ice, focusing on the Laptev Sea. They based the tensile strength on the water depth. The Kara Sea fast ice is particularly interesting in this context because large areas of it only have a weak dependence on the grounding of pressure ridges, evident by the fast ice extending well beyond the shallow areas where grounding is important. Studying the Kara Sea therefore allows us to mostly ignore grounding and focus on the internal ice mechanics necessary for fast-ice formation.

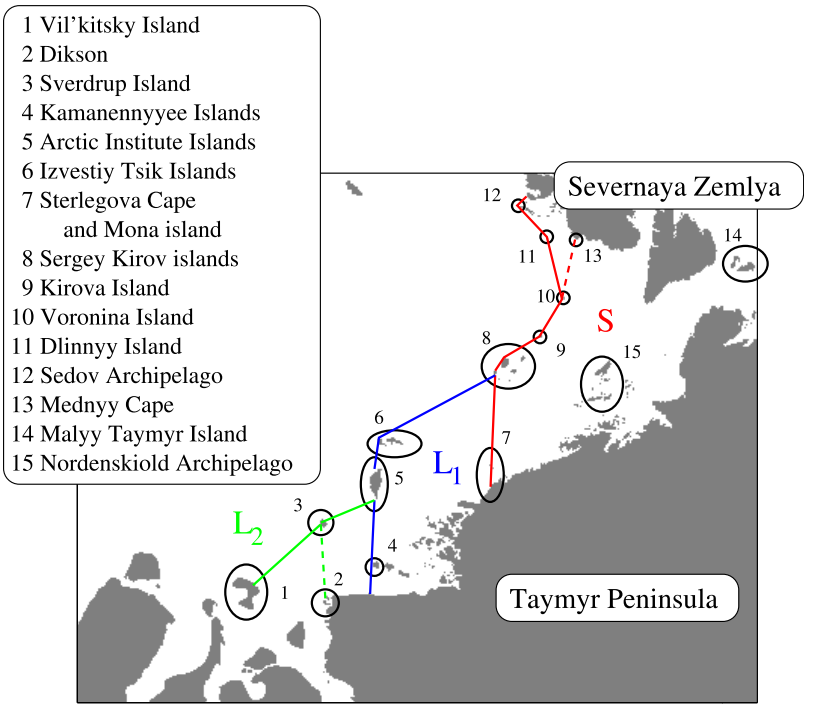

Figure 1. The Severozemelsky region. The lines indicate the typical extent of fast ice for S, L_1, and L_2-modes according to *Divine et al.* [2005], with the dashed lines showing smaller S and L-mode variants. In S-mode the fast ice extends to the red line, in L_1-mode it extends to the outer most boundary of the red and blue lines and in L_2-mode it extends to the outermost boundary of the green, blue, and red lines. Islands and capes important for the fast-ice formation, or otherwise mentioned in the text are marked by a circle.

For the development and testing of the model I focus on the Severozemelsky region in the north-eastern Kara Sea, where fast ice forms over deep waters. The extent of the fast-ice cover in the Severozemelsky region is both large and variable. *Divine et al.* [2003, 2004] showed that the fast ice in this region undergoes significant seasonal and inter-annual variations. *Divine et al.* [2005] then showed that this variability is mostly discrete and that the ice cover in the region primarily occupies one of the three modes shown in Figure 1. More than one mode may be visible each winter, but there is usually one prevalent mode for the entire winter. Which modes occur in a specific year can be linked to the prevailing atmospheric circulation patterns, although that link is somewhat weak [*Divine et al.*, 2005]. All modes follow a chain of islands in the region.

Of these modes the so called S-mode is the smallest, and most common. It extends from Severnaya Zemlya to the Sergey Kirov Islands and from there to Sterlegova Cape. The L_1 and L_2 modes can be considered extensions of the S-mode and only form once the S-mode has been established. In L_1-mode, the fast ice extends from the Sergey Kirov Islands to Izvestiy Tsik Islands and the Arctic Institute Islands and from there onto the coast midway between Dikson and the Pyasina delta through the Kamanennyyee Islands. In L_2 mode, the fast ice extends from the Arctic Institute Islands to Sverdrup Island and from there to Dikson or Vil'kitsky Island.

The mechanism for fast-ice formation appears to mostly depend on local geography. According to *Volkov et al.* [2002] there are two basic mechanisms at work in the Kara Sea. First, grounded pressure ridges stabilize the ice, facilitating fast-ice growth in shallow regions ($\lesssim$25 m). The spatial extent of this ice is then presumably limited by the thickness of the pressure ridge and the ocean depth. Second, further fast-ice growth may occur as ice floes drift onshore and attach themselves onto the coast or fast ice. This second mechanism is the main formation mechanism in the Severozemelsky region since nearly all of the fast ice that forms there forms over waters too deep for pressure ridges to become grounded. *Volkov et al.* [2002] did not specify how this ice remains land fast. However, based on the results of *Divine et al.* [2005] one can assume that during periods of offshore winds, off-shore islands will prevent the ice drift allowing fast ice to form over deep water.

The ice behavior in between the stabilizing islands is therefore of special interest here. *Goldstein et al*. [2004] made a study of the shape of the fast ice boundary in the Bothnian Bay in the Baltic Sea, concluding that the "fast ice boundary is formed of piecewise curved sections" [*Goldstein et al*., 2004, p. 3], or arches. Arch like shapes have also be observed in the Laptev Sea fast ice [*Haas et al*., 2005; *Selyuzhenok et al*., 2015], and *Dumont et al*. [2009] demonstrated the role of arching in forming an ice bridge in Nares Strait.

Arching is a well known phenomenon, of particular interest when it comes to the flow in silos and hoppers, but has also been addressed in sea-ice modeling [see e.g., *Drescher et al*., 1995; *Hibler et al*., 2006; *Matchett*, 2007]. Under the right conditions static arches will form in granular materials passing through openings and converging channels. It has been shown that the strength of the arch depends most crucially on the uniaxial compressive strength of the material, even if the exact formulation of the arch shape and strength may not be simple to deduce [e.g., *Matchett*, 2007]. In a Coulombic rheology uniaxial compressive strength requires tensile strength as well, but this is not the case in general.

Ice arches will thus form in channels and narrow passages due to the ice's nonzero tensile and uniaxial compressive strength. The latter is likely to be a key quantity for determining the strength of the arch. The tensile strength of sea ice is frequently quoted at about 1/20th of the compressive strength [see e.g., *Hibler and Schulson*, 2000; *Wang*, 2007, and references therein]. *Weiss et al*. [2007] suggest that the yield curve (or failure envelope) is scale dependent and scales like $\sqrt{l_1/l_2}$, where l_1 and l_2 are the length of the "stress concentrators" at each scale. They claim this scaling explains the difference between uniaxial compressive strength of about 5 MPa measured in the laboratory and between 150 and 250 kPa measured in situ (values from *Weiss et al*. [2007]). It is not trivial to relate this scaling to the model scale, but given a grid cell size of 10 km one would expect the stress concentrator scale to lie in the range 10 m to 100 m (assuming that the stress concentrator is between two or three orders of magnitude smaller than the scale of the observations, like *Weiss et al*. [2007] do). This gives a scale-appropriate uniaxial compressive strength between 10 and 100 kPa, using the stress concentrator scales and measurements reported by *Weiss et al*. [2007].

In this context it is interesting to note that when *Tremblay and Hakakian* [2006] estimated the strength of fast ice from satellite images and reanalysis data they found the tensile strength to be about half the compressive strength, or about 25 kPa. The reason behind the discrepancy between this value and the commonly quoted 1/20 may be that they did not measure the tensile strength of the ice but rather the strength of the arched structure. In their case the arches presumably form between grounded pressure ridges (in the East Siberian Sea), but the principle is the same as when the arches form between islands, as discussed elsewhere in this text. For an arch forming in a converging channel the strength of the structure is equal to the uniaxial compressive strength [*Matchett*, 2007; *Jenike*, 1961, 1964]. This may not hold here since the arches are not forming in regular, converging channels, but between irregularly spaced pressure ridges. Moreover, due to errors in the reanalysis used and the geostrophic assumption (namely the turning angle) the wind stress will never be perfectly aligned with the thrust delivered to the footers. So on the one hand not all the wind stress is delivered to the arch, meaning that 25 kPa is most likely an upper bound for the uniaxial compressive strength. On the other hand there will be cases where the fast ice breaks because the grounded pressure ridge is freed, not because the arch breaks. In this case assuming the strength of the arched structure is equal to the uniaxial compressive strength is an underestimation.

In the following, it will be assumed that static arching is the key process for fast-ice formation in the Kara Sea. This leads to the discussion of the yield curve in the following section, since uniaxial compressive strength is a necessary condition for arch formation. In section 3, the data used for evaluation of the model are introduced followed by results presented in section 4. The results are discussed in section 5, followed by conclusions.

2. Model Description

2.1. The Kara Sea Ice-Ocean Model

The model used here is a coupled ice–ocean model. The ocean model is the Vector Ocean Model (VOM) developed at the University of Hamburg [see *Backhaus*, 2008] and the ice model is discussed in section 2.2. VOM is a full-fledged primitive equation model with a free surface. The equations for the surface elevation are solved implicitly and for the present set-up both the ice and ocean model use a time step of 600 s. It has a novel z-grid which permits variable vertical grid spacing per ocean column to better represent areas

of steep topography. The coupled model is run at a 10 km horizontal resolution, with the surface and bottom grid cells always 4 m thick and other cells equally thick or thicker. The vertical layer spacing is variable from one column to the next and depends on the steepness of the topography as described in *Backhaus* [2008]. For this particular set-up most of the shallow area of the Kara Sea is resolved with a vertical resolution of 4 m near the bottom and surface and 8 m or 16 m resolution towards the middle of the water column. The simulated area covers all of the Kara Sea and a very small portion of the Barents Sea, west of the Kara Gate. The coupled ice–ocean model has open boundaries just west of the Kara Gate, between the northern tip of Novaya Zemlya and Franz Josef Land, and between the islands of Severnaya Zemlya and Malyy Taymyr.

The model is forced by atmospheric forcing, lateral ocean boundary forcing, and river forcing. The atmospheric forcing is derived from the first National Center for Environmental Prediction/National Center for Atmospheric Research (NCEP/NCAR) reanalysis [*Kalnay et al*., 1996] providing the model with surface air temperatures (at 2 m), total cloud cover, atmospheric pressure, precipitation, relative humidity and winds (at 10 m). Oceanic salinity, temperature, and surface height forcing is derived from results from the NAOSIM model [*Karcher et al*., 2011], a high resolution coupled ice-ocean model of the Arctic and North-Atlantic oceans, forced with the same NCEP/NCAR data. The NAOSIM results were used both for the ocean initial conditions and for forcing on the lateral boundaries. Daily river discharge data for the Ob, Pur, Taz, Yenisey and Nadym were provided upon request by the Global Runoff Data Centre in Koblenz, Germany. Monthly data for Pyasina from June to September as well as the annual average were obtained from the Arctic and Antarctic Research Institute's website. This data is unfortunately no longer available there. River temperatures were interpolated from the measurement data provided by *Lammers et al*. [2007] (using the data they refer to as T_0). The Pyasina river temperatures were set equal to those of its nearest neighbour, the Yenisey, since no temperature measurements were available. Tidal data (M2 component) were superimposed on the sea surface height from NAOSIM, which does not include tides. The tidal data come from the HAMTIDE tidal model and are available from the Integrated Climate Data Center, Hamburg, Germany (http://icdc.zmaw.de/daten/ocean/hamtide.html). The tidal signal was added to the sea surface height derived from the stream function of the NAOSIM model, which has no tides. Tidal variations in the relevant fast-ice areas are small (less than or about 10 cm) and the influence of tides on the simulated fast-ice are negligible.

2.2. The Sea-Ice Model

The sea-ice model is a modification of the viscous-plastic model suggested by *Hibler* [1979] with three layer thermodynamics according to *Semtner* [1976]. The model solves the momentum equation [e.g., *Connolley et al*., 2004]

$$0 = A(\vec{\tau}_a + \vec{\tau}_w) - mf\vec{k}\times\vec{v} - mg\vec{\nabla}H - \mathbf{\nabla}\cdot\boldsymbol{\sigma}, \tag{1}$$

where $\vec{k}$ is a unit vector normal to the surface, $\vec{\tau}_a$ and $\vec{\tau}_w$ are the quadratic air and water stresses, f is the Coriolis factor, g is the gravitational acceleration, $\vec{\nabla}H$ is the gradient of the sea surface height and $\boldsymbol{\sigma}$ is the sea ice stress tensor. This formulation neglects the inertial term. The last term on the right hand side $\mathbf{\nabla}\cdot\boldsymbol{\sigma}$, describes forces due to internal stress while the other terms all represent external forces. The ice is assumed to be isotropic and thus has a yield surface that is a curve in the $\{\sigma_I, \sigma_{II}\}$ plane, where σ_I and σ_{II} are the stress invariants [*Feltham*, 2008]. For stresses inside the yield curve, viscous deformation occurs, while for stresses on the yield curve plastic deformation takes place. In addition a flow rule is used to determine the direction of the plastic strain rate.

Both plastic and viscous behavior can be represented using the stress and strain invariants as [*König Beatty and Holland*, 2010]:

$$\sigma_I = \zeta\dot{\varepsilon}_I - P'(1-k_T)/2 \quad \text{and} \quad \sigma_{II} = \eta\dot{\varepsilon}_{II}. \tag{2}$$

where $\dot{\varepsilon}_I$ and $\dot{\varepsilon}_{II}$ are the first and second invariants of the strain rate tensor. The ζ and η are the nonlinear bulk and shear viscosities, P' is a pressure-like term, and k_T is a tensile strength term, giving the tensile strength as a fraction of the compressive strength. The viscosities are functions of the strain rates and of the compressive strength, which in turn depends on the ice thickness and concentration. The formulation of the viscosities determines the shape of the yield curve.

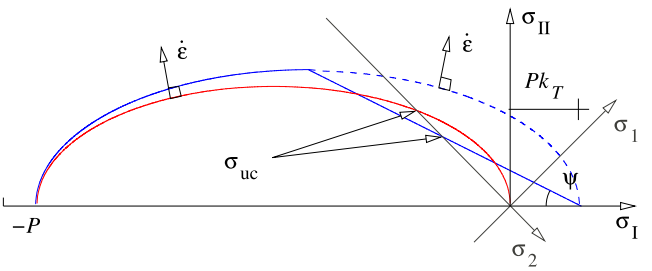

Figure 2. The elliptic (red) and the flexible modified Coulombic (blue) yield curves, plotted in stress invariant space, scaled with the ice pressure P. The principal stress (σ_1 and σ_2) are shown, along with the angle ψ, the tensile strength Pk_T, the uniaxial compressive strength σ_{uc} for each yield curve, and the strain rate $\dot{\varepsilon}$ resulting from the normal flow rule. The blue dashed line shows the plastic potential of the FMC. The angle ψ and the internal angle of friction ϕ are related through the equation $\tan\psi = \sin\phi$.

We will here consider two yield curves, the elliptic yield curve, suggested by *Hibler* [1979] and modified by *König Beatty and Holland* [2010] to include tensile strength, and a more flexible version of the modified Coulombic yield curve suggested by *Hibler and Schulson* [2000] (Figure 2). The viscosities of the elliptic yield curve are given by [*König Beatty and Holland*, 2010]:

$$\zeta = P(1+k_T)/2\Delta \quad \text{and} \quad \eta = \zeta/e^2, \tag{3}$$

where e is the ellipse aspect ratio, P is the ice strength, and

$$\Delta = \sqrt{\dot{\varepsilon}_I^2 + \dot{\varepsilon}_{II}^2/e^2}. \tag{4}$$

These are derived assuming a normal flow rule. It is clear that for small strain rates the viscosity tends to infinity so a lower bound must be set for Δ:

$$\Delta = \Delta_{min}/\tanh\left(\frac{\Delta_{min}}{\sqrt{\dot{\varepsilon}_I^2 + \dot{\varepsilon}_{II}^2/e^2}}\right). \tag{5}$$

Note that Δ_{min} relates to the commonly used maximum viscosity parameter ζ_{max} as $\Delta_{min} = P/(2\zeta_{max})$. This limit is mathematically identical to the continuously differentiable form of the upper bound suggested by *Lemieux and Tremblay* [2009], but is easier to implement when the elliptic yield curve has tensile strength.

The ice strength term, P is defined as:

$$P = P^* h \exp\left(-C[1-A]\right), \tag{6}$$

where P^* is the ice strength parameter, C is a constant, h is the ice thickness, and A the concentration [*Hibler*, 1979]. This is used to calculate η, ζ, and Δ (equations (3) and (5)), following which P' is calculated as:

$$P' = 2\Delta\zeta/(1+k_T). \tag{7}$$

This term is used to calculate σ_I in equation (2). Using P' instead of P in equation (2) prevents the model from producing nonzero stress at zero strain rates [*Ip et al.*, 1991]. The terms P and P' only differ when the bulk viscosity becomes similar to ζ_{max}.

The constants in equation (6) must be chosen empirically, with $P^* \approx 30$ kPa, $e = 2$, and $C = 20$ being common choices [cf. *Hibler*, 1979; *Feltham*, 2008; *Tremblay and Hakakian*, 2006]. Here I use $C = 30$ based on *Bjornsson et al.* [2001]. This is somewhat higher than the more traditional $C = 20$, but it results in sharper gradients in the ice concentration at the down-wind edge of a polynya. Using $C = 30$ instead of $C = 20$ has no effect on the simulated fast ice. The value of P^* is based on the results of *Tremblay and Hakakian* [2006], who estimated the strength of the ice under isotropic compression, p^*, which relates to P^* as:

$$P^* = \frac{2p^*}{1-k_T+\sqrt{(1+1/e^2)(1+k_T)^2}}. \tag{8}$$

I choose $p^* = 40$ kPa for all the experiments run here, which gives $P^* = 37.8$ kPa for $e = 2$ and $k_T = 0$. This value is slightly higher than the mean value reported by *Tremblay and Hakakian* [2006], in order to compensate for the expected low bias from their method. I also use 1.5×10^{-3} as the atmospheric drag coefficient. This is compatible with the one *Tremblay and Hakakian* [2006] use when taking into account that I use surface winds but they used geostrophic winds.

Finally we note that the uniaxial compressive strength of the elliptic yield curve is (see Appendix A for details):

$$\sigma_{uc} = \frac{-4p^* k_T \sin\phi}{(1-\sin\phi)(1-k_T+\sqrt{(1+\sin^2\phi)(1+k_T)^2})}. \quad (9)$$

The other yield curve considered here is the flexible modified Coulombic yield curve (FMC), which is a reformulation of the yield curve proposed by *Hibler and Schulson* [2000]. The FMC is a modification of the elliptic yield curve, replacing the elliptic shape with a Coulombic branch for $\sigma_I > -P(1-k_T)/2$. In this case the flow rule is nonassociated for the Coulombic branch, with the plastic potential defined by the ellipse.

Using the stress and strain rate invariants from equation (2) it is easy to derive the Coulombic branch as the line

$$\sigma_{II} = -(\sigma_I - Pk_T)\sin\phi, \quad (10)$$

where ϕ is the macroscopic angle of friction [see e.g., *Tremblay and Mysak*, 1997]. Now since $\sigma_{II} = \eta\dot{\varepsilon}_{II}$ this gives η_1, the shear viscosity for the Coulombic branch of the yield curve:

$$\eta_1 = -\frac{(\sigma_I - Pk_T)\sin\phi}{\dot{\varepsilon}_{II}} \quad (11)$$

$$= \frac{P(1+k_T)/2 - \zeta\dot{\varepsilon}_I}{\dot{\varepsilon}_{II}}\sin\phi. \quad (12)$$

The transition between the elliptic and Coulombic branches occurs when $\sigma_I = -P(1-k_T)/2$, for which $\sigma_{II} = P(1+k_t)/(2e)$, since e is the ellipse axis ratio. From these two equations and equation (10) above, we can write:

$$\sigma_{II} = P\frac{1+k_T}{2e} \quad (13)$$

$$= -(\sigma_I - Pk_T)\sin\phi \quad (14)$$

$$= P\frac{1+k_T}{2}\sin\phi, \quad (15)$$

which gives

$$e = 1/\sin\phi. \quad (16)$$

This ensures that the yield curve is continuous.

The resulting equations for the shear and bulk viscosities are

$$\zeta = P(1+k_T)/2\Delta, \quad (17)$$

$$\eta = \min\left(\zeta\sin^2\phi, \frac{P(1+k_T)/2 - \zeta\dot{\varepsilon}_I}{\dot{\varepsilon}_{II}}\sin\phi\right), \quad (18)$$

$$\Delta = \Delta_{min}/\tanh\left(\frac{\Delta_{min}}{\sqrt{\dot{\varepsilon}_I^2 + \dot{\varepsilon}_{II}^2\sin^2\phi}}\right). \quad (19)$$

The FMC allows for easily adjusting both the macroscopic angle of friction and the amount of tensile strength.

Finally we note that the uniaxial compressive strength of the FMC yield curve is (see Appendix A for details):

$$\sigma_{uc} = -2p^* \frac{1-k_T+\sqrt{(1-k_T)^2+4(1+e^2)k_T}}{(1+e^2)(1-k_T+\sqrt{(1+1/e^2)(1+k_T)^2})}. \quad (20)$$

In order to solve the momentum equation I use a successive over relaxation (SOR) method on a linearization of the nonlinear equations and a spatial discretization on a C-grid, the same as the ocean model uses. The choice of discretization (in particular between C and B-grid) is known to affect the solution in boundary

flows and flows along narrow channels [*Bouillon et al.*, 2009], but this is not addressed here. To linearize the problem one must use the velocities from the previous time step to calculate the nonlinear terms in $\nabla \cdot \boldsymbol{\sigma}$. The resulting velocities will be erroneous due to the poor representation of the nonlinear effects in this procedure, so repeating the linearization and solve to produce a better velocity estimate is a common practice [*Zhang and Hibler*, 1997; *Lemieux and Tremblay*, 2009]. Here I repeat the linearization and linear solve an arbitrary number of times using the following algorithm:

for $k = 1$ to n_{OL} **do**
  Calculate viscosities based on $\vec{v}^{k-1}$
  $\vec{v}^{k} \leftarrow$ solution to the linear system
 if $k > 1$ **then**
  $\vec{v}^{k} \leftarrow (\vec{v}^{k} + \vec{v}^{k-1})/2$
 end if
 $\epsilon \leftarrow \max(|v^{k} - v^{k-1}|)$
 if $\epsilon < \epsilon_{\mathrm{OL}}$ **then**
  exit loop
 end if
 $\epsilon_{\mathrm{SOR}} \leftarrow \alpha\epsilon$
 end for
$\epsilon_{\mathrm{SOR}} \leftarrow \max(\epsilon_{\mathrm{OL}}, |v^{k} - v^{0}|)$

where α is a constant of proportionality controlling the speed with which a progressively more accurate solution is demanded from the SOR solver. Its role is discussed further below.

This algorithm assumes an upper limit on the number of outer loops, n_{OL}. This is necessary since the condition $\epsilon < \epsilon_{\mathrm{OL}}$ may not be met within a reasonable number of outer loops and the solver therefore does not fully converge at every time step. Using $\epsilon_{\mathrm{OL}} = 10^{-4}$ m/s and a time step of $\Delta t = 600$ s the fraction of fully converged time steps reaches an asymptote of about 95% at about $n_{\mathrm{OL}} \gtrsim 500$. I therefore use $n_{\mathrm{OL}} = 500$ from here on out, since using more iterations only results in marginal gains in accuracy. Using much smaller values for ϵ results in prohibitively long model run times while using much larger values results in errors in the solution which break up the fast ice. This algorithm therefore requires the outer-loop error to be less than 10^{-4} m/s, as long as the number of outer loops is less than 500. Viscosities are calculated based on the chosen yield curve (equations (3) and (5) for the ellipse and 17, 18, and 19 for the FMC). When $k = 1$ velocities from the previous time step, $\vec{v}^{0}$, are used. This algorithm is similar to that used by *Lemieux and Tremblay* [2009], except they use a GMRES solver instead of the SOR solver used here.

The SOR solver is considered to have converged when the maximum change in velocity between consecutive SOR steps is less than ϵ_{SOR}. In traditional SOR implementations ϵ_{SOR} is a constant, but here it is always proportional to the outer-loop error, with a constant of proportionality $\alpha = 1/10$. For the first SOR solution the outer-loop error is unknown and so the maximum velocity difference between the two previous time steps is used. Using a variable exit condition vastly improves the global convergence of the method, compared to using a constant ϵ_{SOR}.

3. Observational Data

The Arctic and Antarctic Research Institute (AARI) and the National Snow and Ice Data Center (NSIDC) have jointly published sea-ice charts produced by the AARI from 1933 to 2006, with no observations during 1993–1996 [*Arctic and Antarctic Research Institute*, 2007]. The charts were produced for safety of navigation in the polar regions and for other operational and scientific purposes. They show ice concentration for multiyear ice, first year ice, new/young ice and land-fast ice. Historically the charts were compiled from many different sources, but the latest charts (i.e., after 1996) are mostly derived form satellite observations. In addition to these observations from ships, polar meteorological stations, and air reconnaissance flights were used to compile the charts.

Chart coverage and frequency varies, but for most of the series charts were compiled every 10 days during the navigation season, and monthly for the rest of the year. Most of the time a single chart will cover a

given 10 day period, i.e., days 1–10, 11–20, and 21 until the end of the month, for each month. Sometimes more than one chart is given for each period, in which case indication is given whether the majority of the data in the chart was collected early or late in the observation period. The more recent charts (i.e., after 1996) cover more area than the older ones and are more frequent.

The satellite-derived polynya data used here are the same as that used in *Kern et al*. [2005]. Open water and thin-ice extent of a polynya is estimated using the Polynya Signature Simulation Method (PSSM) developed by *Markus and Burns* [1995] and *Hunewinkel et al*. [1998]. The PSSM is based on Special Sensor Microwave/Imager (SSM/I) brightness temperature polarization ratios at frequencies of 37 and 85 GHz. The PSSM data are available from the beginning of October through May and as such covers most of the fast-ice period. The PSSM classifies pixels as open water, covered with newly formed thin ice, or covered with thick ice.

Although the PSSM data does not show fast ice directly, it is useful in this context as it shows clearly flaw polynyas that form downwind of the fast ice. The data therefore allow one to verify the AARI fast-ice data, as long as the weather conditions are suitable.

The AARI charts will be the primary source of data for model evaluation, being the only available fast-ice data set for the region. In this particular study I will focus on a single winter only, namely on 1997–1998. I choose this winter because it is in the latter part of the AARI data set which has better temporal resolution and spatial cover than the earlier period. The winter 1997–1998 is also the first entire winter in that period and so I use it to reduce as much as possible the effects of the underlying warming trend in the Arctic.

The temporal evolution of the fast-ice cover can be visualized by studying the AARI observations. In Figure 3, the left plot shows the date around which stable land-fast ice was observed to form in 1997–1998 and the right plot shows the last date around which fast ice was observed in summer 1998.

According to the observations fast ice in the Severozemelsky region formed in two discrete jumps in 1997–1998. Initially, fast ice formed inland of the Nordenskiöld Archipelago during the 1–10 November observation period (this date is outside the temporal range of Figure 3), growing only slightly after the initial formation. The 1–10 January observation then shows a fully formed S-mode fast ice. This is subject to some very minor partial break-ups and recoveries, but remains mostly unaltered until the summer break-up.

Summer break-up of the Severozemelsky fast ice occurs in the period from 11 July to 11 August, after which no fast ice is observed in the region. Fast ice in the Vilkitsky Strait breaks up first, followed by the rest of the Severozemelsky fast ice offshore off the Nordenskiöld Archipelago. The fast ice inland of the Nordenskiöld Archipelago is the last to break up at the beginning of August, having remained land fast for 9 months.

4. Model Results

In this section, a series of experiments using the elliptic and FMC yield curves are described. For each experiment the model is initialized using the model state from 5 October 1997. On that date the model domain is virtually ice free so the role of ice dynamics is negligible. The model is then run until summer 1998 with output of daily snapshots of key model variables. In order to maximize the accuracy of the model results I always use $n_{OL}=500$ as the maximum number of outer-loop iterations, unless otherwise stated.

The extensive observations of the Kara Sea land fast ice provided by *Arctic and Antarctic Research Institute* [2007] allows us to easily define criteria by which one can judge the quality of the model results. It is important in this context that the fast-ice cover is very stable, exhibiting one of the three modes described earlier nearly every winter. The S or L-mode fast ice usually forms at the end of December or start of January, breaking up in late June or in July. This can be used to state model evaluation criteria applicable to any model of the Kara Sea land-fast ice, regardless in particular of whether the model runs for one or more years.

The most important criterion for model evaluation is whether the fast ice forms in one of the modes and whether realistic flaw polynyas form at its edge. The extent of the modes themselves is determined by the topography, so capturing one of the S or L-modes, as opposed to some other configuration should be easy, assuming realistic fast ice forms in the model at all. The timing of fast-ice formation and break-up is probably more difficult to capture. This timing depends on the growth and melt rates of the ice and the timing of freeze up and melt, and may be heavily influenced by the applied forcing. One would, however, expect

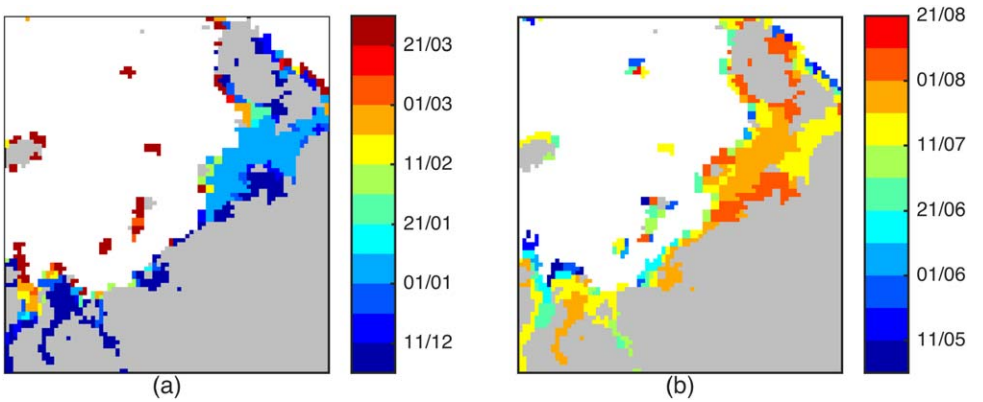

Figure 3. Time of onset of a stable fast ice cover in early winter (a) and time when fast ice is last observed in summer (break-up) (b) in the Severozemelsky region. Data from the *Arctic and Antarctic Research Institute* [2007].

the model to be able to reproduce the observed formation and break-up times to within the observed variability, which is about a month. Finally, capturing the observed mode at the time it is observed is probably the most difficult since whether an S or an L-mode forms depends somewhat weakly on the atmospheric state.

4.1. The Elliptic Yield Curve

Let us first consider the elliptic yield curve proposed by *Hibler* [1979], since this is by far the most common yield curve used today. Using this yield curve with its commonly used parameters very little land-fast ice is modeled. Increasing tensile strength only produces land fast ice once $k_T \gtrsim 0.8$, which is much higher than the expected 1/20. The model does, however, produce stable S-mode land-fast ice when ζ_{max} is increased sufficiently, even without any tensile strength. The reason appears to be that the elliptic yield curve allows uniaxial compressive stress, i.e., the modeled stress state can lie in the positive principal stress quadrants. Due to its peculiar shape, uniaxial compressive strength therefore exists when using an elliptic yield curve, even if no tensile strength is present. Increasing ζ_{max} also allows the modeled ice to remain plastic for lower strain rates, which is important since plasticity is a necessary condition for arch formation.

Let us now explore the relationship between the maximum viscosity and fast ice formation. To do this I ran a set of experiments changing ζ_{max} from $(10^8\text{s})P$ to $(10^{17}\text{s})P$ in steps of factor 10. For each experiment I calculate the maximum modeled fast ice area in the Severozemelsky region (Figure 4) on 14 April, which is at the peak of the fast ice season. On that date a strong offshore wind creates a clear flaw polynya making the identification of land-fast ice easy (Figure 5). In this case I consider any ice moving slower than a critical velocity of 10^{-4} m/s as being land fast. Ice moving at that speed crosses a third of a grid cell in one year. The results are not sensitive to the choice of critical velocity.

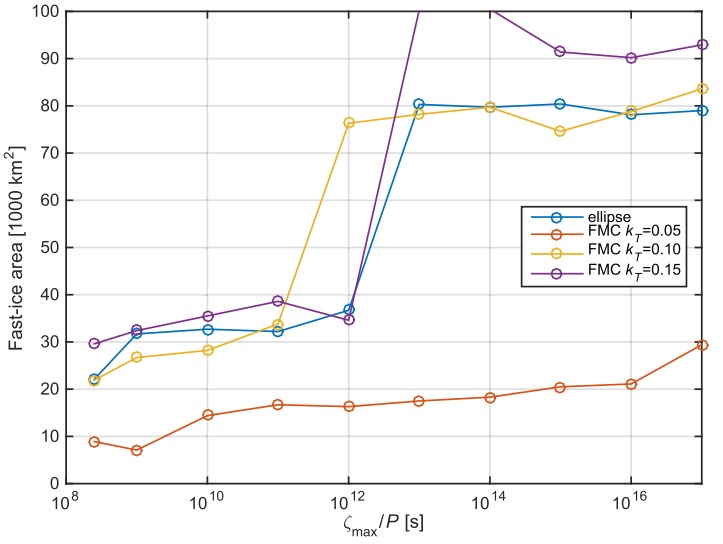

Figure 4. Maximum modeled fast-ice area in the Severozemelsky region as a function of the maximum viscosity (ζ_{max}/P) for the elliptic yield curve and the FMC with $\phi = 45^\circ$ and three different values for k_T.

The modeled fast ice area increases as ζ_{max} is increased, reaching its maximum extent for $\zeta_{max} \geq (10^{13}\text{s})P$. The increase in fast ice area comes

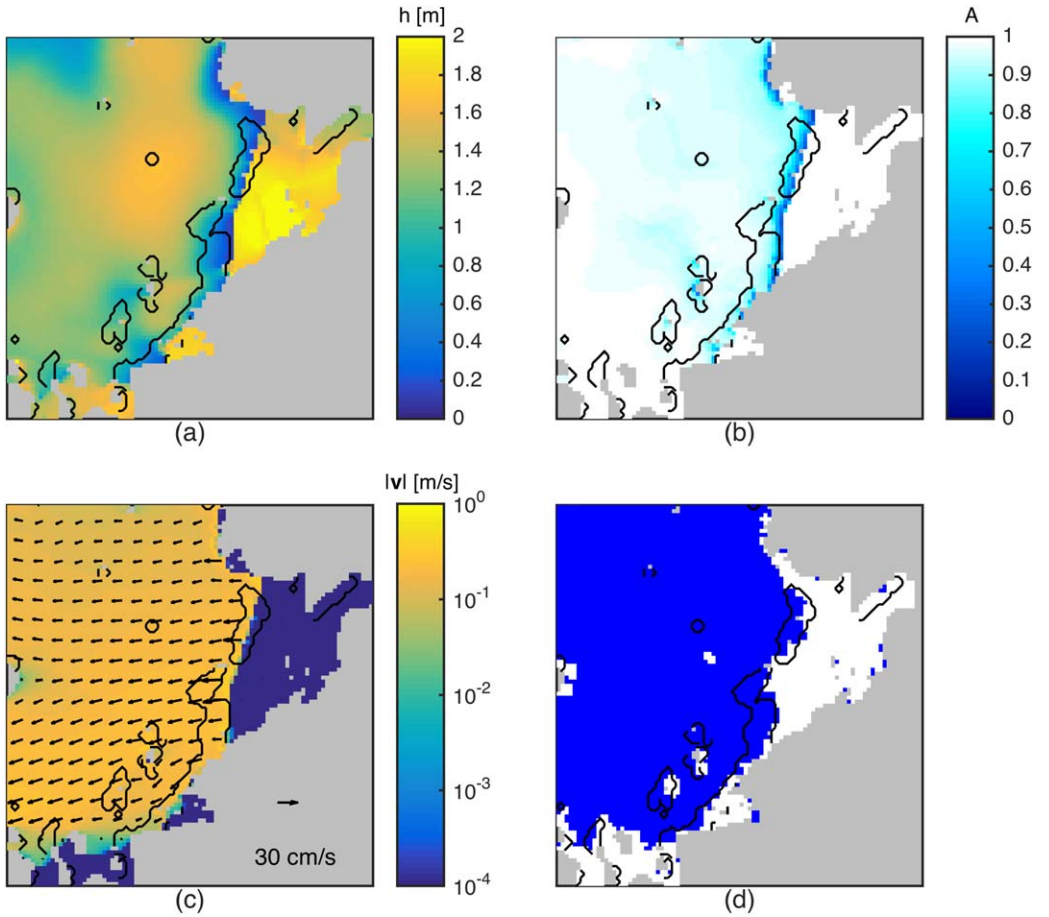

Figure 5. Simulation results using the elliptic yield curve with $\zeta_{max} = (10^{13}\text{s})P$: (a) ice thickness (capped at 2 m), (b) ice fraction, and (c) ice velocities on a logarithmic scale. The snapshot is taken after the first time step of 14 April. (d) The observed fast ice from the AARI observations covering the period from 10 to 17 April. The lines show the extent of newly formed ice and open water from the PSSM. The observations have been interpolated onto the model grid.

in discrete jumps as fast ice only forms behind arches forming between islands. Larger values of ζ_{max} appear to allow the ice to form larger stable arches, capable of spanning larger gaps between islands in the Severozemelsky region. Setting ζ_{max} larger than $(10^{13}\text{s})P$ does not alter the modeled maximum fast ice area.

In general it is preferable to keep the maximum viscosity as low as possible, since this makes the equation of motion easier to solve. The lowest feasible value for ζ_{max} should therefore be chosen. In this case it is $\zeta_{max} = (10^{13}\text{s})P$, giving fast-ice extent of 79, 900 km^2, close to the observed value of 83, 000 km^2. The difference between the modeled and observed areas is due to the fact that in the model the fast ice connects with Severnaya Zemlya at Mednyy Cape, while in reality it reaches the Sedov Archipelago. The modeled configuration is therefore realistic, even though it differs from the observed one (see Figure 1).

In the tests performed here stable fast ice did not form in the model when using two outer-loop iterations, as is common practice. This was also the case when halving the model time step from 600 s to 300 s. Increasing the number of outer loops increases the accuracy of the solution and reduces the chances of spurious errors in the solution breaking up the fast ice. It is therefore not possible to quantify how many outer-loop iterations are needed to ensure a stable fast-ice simulation, especially since the algorithm is unable to reach a fully converged solution for every time step. More outer-loop iterations only reduce the odds that a spurious error breaks up the simulated fast ice. The solver used here converges for about 95% of all model time steps for $n_{OL} \gtrsim 500$.

In order to show the temporal evolution of the fast-ice area I calculate the 5 day fast-ice area using the 5 day mean ice speed. The 5 day fast-ice area is then the area of ice where the 5 day mean speed is less than

or equal to 10^{-4} m/s. Ice traveling at this speed crosses a third of a grid cell in one year. It is necessary to average the ice speed in some way, since otherwise short periods of calm winds causing no ice movement would cause an overestimation of the fast-ice area. The method I use here is the same as *Lemieux et al.* [2015] use, except they use biweekly means and 5×10^{-4} m/s for the critical speed. Using their criterion gives virtually identical results here, only with a lower temporal resolution. Figure 6 shows such a time series of fast-ice area for the observations and the elliptic yield curve using $\zeta_{max}=(2.5\times10^{8}\text{s})P$ and $\zeta_{max}=(10^{13}\text{s})P$.

In the AARI observations fast ice starts forming in and around the Nordenskiöld Archipelago in early November. This is not captured by the model. An S-mode then forms at the start of January and remains stable until the start of August when it rapidly breaks up. In the model an S-mode starts forming in January, but this is not stable and breaks up again towards the end of the month. The wind is very calm and primarily onshore during most of February. This causes the algorithm used here to report unrealistically large simulated fast ice area in February, making a reliable automated estimation of the fast ice area impossible for most of the month. An S-mode is clearly established in the model in early March and this remains stable until mid-May. An S-mode forms again at the start of June, but this is not very stable and breaks up completely towards the end of the month. A visual inspection of the daily snapshots confirms this analysis, showing a clear flaw polynya forming during the period of March–April (figure 5) and clear on- and offshore ice flow during the simulated break-ups in January/February and mid-May, respectively (Figure 7).

A comparison between the model results and the PSSM observations can only be made when a clear polynya forms in the observations. A good example of a flaw polynya forming in both the model and observations occurs on 14 April, and is shown in Figure 5, confirming the good results of the model at that time. The PSSM observations can also be used to confirm that the simulated break-up in mid-May is not realistic, since the observations show a clear flaw polynya, but a small coastal polynya forms in the model (not shown). A small flaw polynya can also be seen in the PSSM observations on 19 and 23 January (not shown), confirming that the simulated break-up of fast ice in late January is also not realistic either.

4.2. Sensitivity to the Parameters of the Elliptic Yield Curve

Let us now consider what effects changing the tensile strength, aspect ratio, and compressive strength of the elliptic yield curve has. Starting with increased tensile strength I ran experiments changing k_T from 0.01 to 0.1 in steps of 0.01. In this case stable fast ice with virtually the same characteristics as described earlier formed for $k_T \leq 0.06$. This corresponds to a tensile strength of $T \leq 2.2$ kPa and uniaxial compressive strength in the range 15kPa $\leq \sigma_{uc} \leq$ 18 kPa. The fast-ice area increases by about 10, 000 km^2 during the stable period from March to mid-May with increased uniaxial compressive strength. This is well within the observed variability of the S-mode area. For $k_T > 0.06$ an unrealistic polynya forms mid-April, as shown in Figure 8 for $k_T=0.08$. In this case an arch appears to extend from the Sergey Kirov Islands to two islands not shown in Figure 1: Uedineiya, in the middle of the figure and Vize, towards the figure's top.

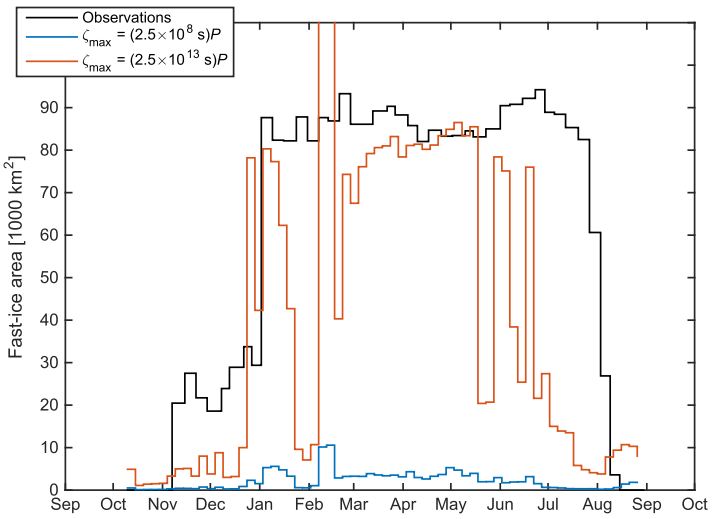

Figure 6. Time series of fast-ice area in the Severozemelsky region form the AARI observations and the model with $\zeta_{max}=(2.5\times10^{8}\text{s})P$ and $\zeta_{max}=(10^{13}\text{s})P$, using the elliptic yield curve with $p^*=40$ kPa, $e=2$, and $k_T=0$. The model results shown here are 5 day means as described in the text.

Dumont et al. [2009] demonstrated that changing the aspect ratio of the ellipse affects the way an ice bridge in a converging channel forms. This is also the case here, demonstrated by changing e from 1 (a circle) to 2.5, in steps of 0.1. Stable fast ice with virtually the same characteristics as those

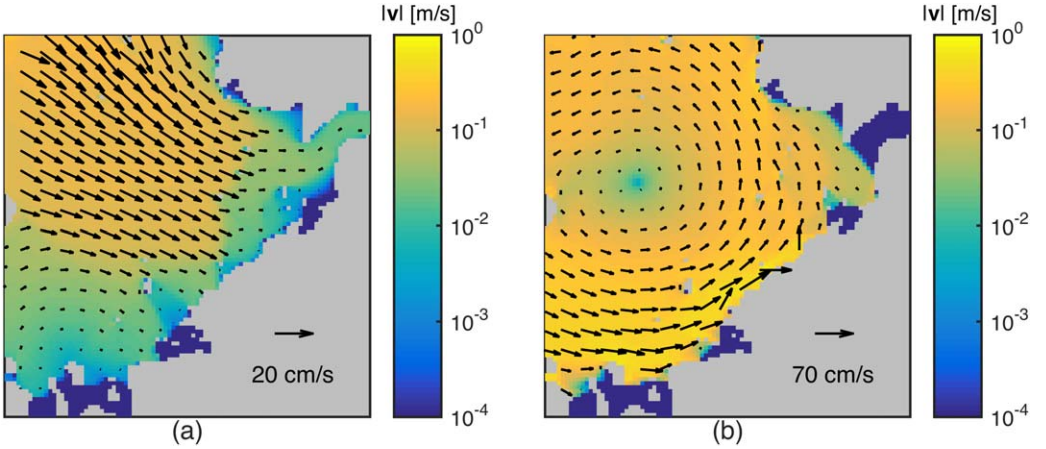

Figure 7. Ice speed using the elliptic yield curve with $\zeta_{max} = (10^{13}\text{s})P$, $p^* = 40$ kPa, $e = 2$, and $k_T = 0$ on (a) 1 February and (b) 22 May.

described in section 4.1 forms for $1.3 \leq e \leq 2.1$. This corresponds to uniaxial compressive strength in the range $14\text{kPa} \leq \sigma_{uc} \leq 26\text{kPa}$. Using a larger e (a flatter ellipse) results in no or unrealistically little fast ice forming, while using a smaller e (a more round ellipse) results in an unrealistic polynya formation, similar to the one in Figure 8. The fast-ice area increases in a similar manner as before with increased uniaxial compressive strength. Note that using $e = 1.3$ the fast ice does not break up in mid-May, but remains land fast until the end of July. Using $e = 1.3$, however, the fast ice forms an L-mode and not the observed S-mode (see Figure 9).

The uniaxial compressive strength of the ellipse depends on its biaxial compressive strength. To test the relationship between the biaxial compressive strength, p^* and fast-ice formation I ran experiments changing p^* from 30 kPa to 45 kPa, the range suggested by *Tremblay and Hakakian* [2006]. In this case stable fast ice with the same characteristics as before was present in the model for $p^* \geq 38$ kPa, which corresponds to $P^* \geq 35.9$ kPa and a uniaxial compressive strength of $\sigma_{uc} \geq 14$ kPa. The fast-ice area increases the same as before as the uniaxial compressive strength increases. Extending the range of p^* up to 55 kPa still produced stable and realistic land-fast ice, despite being outside the range proposed by *Tremblay and Hakakian* [2006]. It is likely that such high compressive strength would result in adverse effects on other model aspects, but this was not investigated. Assuming that the maximum uniaxial compressive strength is about 25 kPa one would have to set $p^* \gtrsim 65$ kPa to see unrealistic polynya formation as described above. This is well outside the probable range given by *Tremblay and Hakakian* [2006] and was not attempted here.

4.3. Flexible Modified Coulombic Yield Curve

Now consider the flexible variant of the modified Coulombic yield curve, the FMC, introduced in section 2.2. I tested the FMC using $\phi = 30^\circ$ (as suggested by *Tremblay and Mysak* [1997]) and $\phi = 45^\circ$, and k_T ranging from 0.05 to 0.3. Let us first consider $\phi = 30^\circ$. In this case stable fast ice with the same characteristics as before forms for $0.16 \leq k_T \leq 0.25$, with increasing fast-ice area for increasing k_T, in the same manner as before. This corresponds to a tensile strength between 6.0 kPa and 9 kPa, and uniaxial compressive strength between 4.4 kPa and 18 kPa. Using a lower value for k_T results in no or unrealistically little fast ice and using a larger k_T results in an unrealistic polynya, similar to the one described before. As with the ellipse, here the fast-ice area increases by about 10, 000 km^2, during the stable period from March to mid-May, with increased uniaxial compressive strength.

Using $\phi = 45^\circ$ gives higher shear strength and thus a higher uniaxial compressive strength for the same tensile strength, compared to using $\phi = 30^\circ$ (consider Figure 2 and equation (20)). This shows in the results, with stable fast ice forming with the same characteristics as before for $0.09 \leq k_T \leq 0.13$ when ϕ is set to 45°. This corresponds to a tensile strength between 3.3 kPa and 4.9 kPa and uniaxial compressive strength between 16 kPa and 22 kPa. The fast-ice area increases as the uniaxial compressive strength increases, in a very similar manner as when using $\phi = 30^\circ$.

Let us now consider again the effect of changing ζ_{max}, but this time when using the FMC. To get a sense of the effect of this Figure 4 shows the fast-ice area on 14 April for the FMC using $\phi = 45^\circ$ and k_T equal to 0.05,

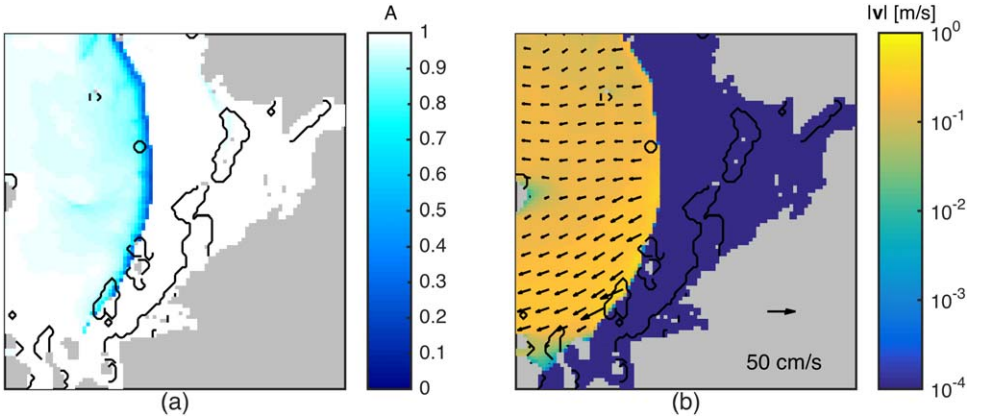

Figure 8. Simulation results using the elliptic yield curve with $\zeta_{max}=(10^{13}\text{s})P$, $p^*=40$ kPa, $e=2$, and $k_T=0.08$: (a) ice fraction and (b) ice speed. The lines show the extent of newly formed ice and open water from the PSSM. The observations have been interpolated onto the model grid. The snapshot is taken after the first time step of 14 April.

0.1, and 0.15. These k_T values are below, in the middle of and above the range of k_T that produces realistic fast ice with $\zeta_{max}=(10^{13}\text{s})P$. Using $k_T=0.05$ gives the commonly used fraction of 1/20, while $k_T=0.15$ gives a uniaxial compressive strength of $\sigma_{uc}=25$ kPa, a likely upper bound. In this set-up very little fast-ice is produced for $k_T=0.05$ and the model behavior for $k_T=0.1$ is very similar to that when using the ellipse, except realistic fast ice forms for $\zeta_{max} \geq (10^{12}\text{s})P$. With $k_T=0.15$ the behavior is again similar for $\zeta_{max} < (10^{13}\text{s})P$, but for $\zeta_{max}=(10^{13}\text{s})P$ and $\zeta_{max}=(10^{14}\text{s})P$ too much fast ice forms, as noted before (see Figure 8). For larger ζ_{max} values realistic S-mode fast ice forms again.

5. Discussion

In the section 4, I outlined experiments where different yield curves were used to model land-fast ice in the Kara Sea in a realistic set-up. Realistic fast-ice extent and polynya formation could be modeled using both the commonly used elliptic yield curve and the FMC. Stable fast ice forms in the model only when the uniaxial compressive strength of the yield curve is in the range $15\text{kPa} \lesssim \sigma_{uc} \lesssim 20$ kPa (see Table 1 for details) and the maximum viscosity is at least $\zeta_{max}=(10^{13}\text{s})P$. A more accurate solver than the traditional single pseudo-time step approach is also necessary. The solver used here is consider converged when the residual norm is less than $\epsilon_{OL}=10^{-4}$ m/s, but the sensitivity of the solution to ϵ_{OL} was not investigated. The solver converges in 95% of the model time steps.

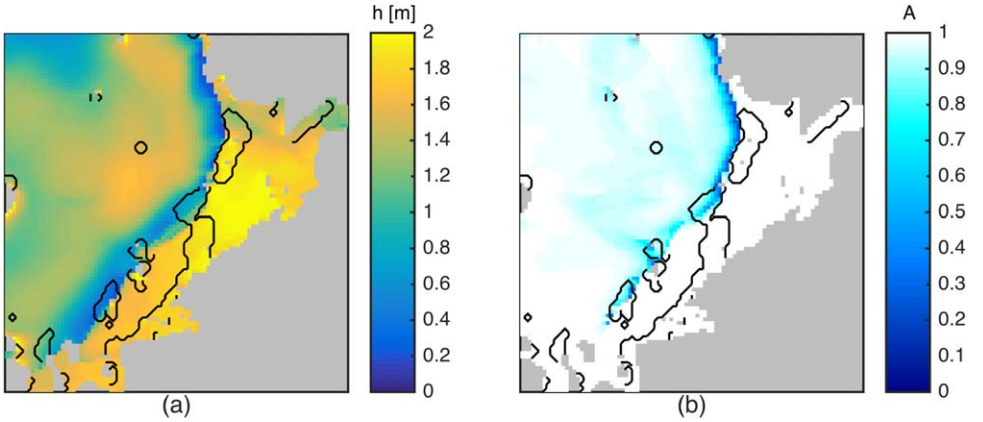

Figure 9. Simulation results using the elliptic yield curve with $\zeta_{max}=(10^{13}\text{s})P$ and $e=1.3$: (a) ice thickness (capped at 2 m) and (b) ice fraction. The lines show the extent of newly formed ice and open water from the PSSM. The observations have been interpolated onto the model grid. The snapshot is taken after the first time step of 14 April.

Table 1. Yield Curve Parameters for Which Stable Fast Ice Forms in the Model

Yield Curve Shape	Parameter Range	Uniaxial Compressive Strength (kPa)
Ellipse ($e = 2$)	$0 \leq k_T \leq 0.06$	$15 \leq \sigma_{uc} \leq 18$
Ellipse ($k_T = 0$)	$1.3 \leq e \leq 2.1$	$14 \leq \sigma_{uc} \leq 26$
Ellipse ($e = 2$, $k_T = 0$)	$P^* \geq 36$ kPa	$\sigma_{uc} \geq 14$
FMC (ϕ=30°)	$0.16 \leq k_T \leq 0.25$	$4.4 \leq \sigma_{uc} \leq 18$
FMC (ϕ=45°)	$0.09 \leq k_T \leq 0.13$	$16 \leq \sigma_{uc} \leq 22$

One of the main results is that in order to produce fast ice in the model the maximum viscosity, ζ_{max} must be set to at least $\zeta_{max}=(10^{13}\text{s})P$, rather than $\zeta_{max}=(2.5\times10^{8}\text{s})P$, which is commonly used. The fact that such a large maximum viscosity is needed to raise the question of what the appropriate value for ζ_{max} should be. The commonly used maximum viscosity comes from *Hibler* [1979], and was "chosen to be large enough to be rarely reached so that [it does] not significantly affect the computations" [*Hibler*, 1979]. This limit allows plastic behavior for deformation rates larger than about 10^{-4} day^{-1}. This is a reasonable limit for the central pack ice, and it is not unreasonable to assume that a lower limit is needed when simulating land-fast ice. Setting $\zeta_{max}=(10^{13}\text{s})P$, as is done here allows plastic behavior for deformation rates larger than about 10^{-9} day^{-1}.

One could also imagine relating the maximum viscosity in the model to the viscous creep (or secondary creep) of sea-ice. Such creep is usually described using Glen's law in which strain rate is proportional to the stress cubed and can therefore not be directly related to the viscous response of the viscous-plastic model [e.g., *Timco and Weeks*, 2010]. The measurements of *Richter-Menge and Cox* [1995] do, however, indicate that for low stress (less than 0.1 MPa) the relationship may become linear. Should this be the case then the viscous response of the viscous-plastic model is realistic. Measuring viscous creep for stresses as low as those in question here (around 0.1 Pa) is, however, very difficult and the author is not aware of any such measurements. There seems therefore not to be a simple answer to the question of what the appropriate value for ζ_{max} is. A more detailed investigation of this point should be considered outside the scope of the current study.

Another important result is that the model simulates realistic fast ice in the middle of winter using either of the two yield curves tested, as long as the uniaxial compressive strength of the yield curve is sufficient and not too large. Table 1 lists all the different experiments and shows that for uniaxial compressive strength in the range 15kPa$\lesssim\sigma_{uc}\lesssim$20 kPa the model simulates realistic fast-ice extent and flaw polynyas. A notable exception is that when using the FMC with ϕ=30°, realistic fast ice forms for as little as σ_{uc}=4.4 kPa (with k_T=0.16). A probable reason is that for such a small angle, the tensile strength in the model is considerable, even if the uniaxial compressive strength is small. In this case the ice can remain land-fast through a combination of the uniaxial compressive and tensile strengths. When the uniaxial compressive strength is too small, little or no fast ice forms in the model. If it is too large, the simulated ice becomes capable of forming over large arches and the fast ice becomes more extensive than that observed (Figure 8).

The appropriate uniaxial compressive strength for the model of 15kPa$\lesssim\sigma_{uc}\lesssim$20 kPa is somewhat smaller than the 25 kPa observed by *Tremblay and Hakakian* [2006] and reported as the ice tensile strength. This is a very good result if 25 kPa is indeed an upper bound, as has already been suggested. The model value also compares reasonably well with the observations and scaling arguments presented by *Weiss et al*. [2007]. Note also that since these arches do not form in converging channels but rather in a complex, potentially interacting manner, the strength reported by *Tremblay and Hakakian* [2006] may not be simply the uniaxial compressive strength, or an upper bound thereof. A more detailed investigation, and potentially simulation of the scenes investigated by *Tremblay and Hakakian* [2006] is needed to determine this.

In general the model's good performance strongly supports the supposition that fast-ice formation in the Kara Sea can be attributed to arch formation between the many islands in the Severozemelsky region. Note that arches have been observed to form between grounded pressure ridges supporting land-fast ice [*Goldstein et al*., 2004; *Selyuzhenok et al*., 2015; *Haas et al*., 2005]. The mechanism suggested herein should be equally applicable to arches forming between islands and arches forming between grounded pressure ridges, although this has not been investigated here, in the latter case the footers of the arches are much weaker and the resulting arches also much smaller.

The model therefore does a good job at simulating the fast-ice extent at the peak of the fast-ice season, one of the two main evaluation criteria we can test here. The other is whether the timing of formation and break-up is correct and for most set-ups the model does not fair as well on this criterion. Only one set of

parameters allowed the model to simulate a realistic fast-ice extent and break-up time. The realistic break-up time was simulated using the elliptic yield curve and $e = 1.3$. For this set-up the land-fast ice formed an L-mode and not the observed S-mode. None of the model parameter settings allowed the model to produce realistic fast-ice extent and formation times.

Partial break-ups and reformations may not be unrealistic and according to *Volkov et al*. [2002] the Severozemelsky fast ice may be subject to partial break-ups throughout winter. According to the AARI observations, however, only very small partial break-ups occurred in the winter 1997–1998. This is supported by the PSSM data which only shows flaw polynyas during the fast ice season of 1997–1998 and no coastal polynyas within the fast-ice area. The temporal resolution of the AARI charts is only about 10 days and so it is possible that break-ups may occur and the fast ice reforms in between observations. In the model, however, the fast ice has usually not reformed within 10 days of a break-up.

If we consider the entire observational period then the observed fast ice also seems to be more stable than the modeled one. Break ups and reformations are visible in the AARI observations during the formation phase in the winters of 2002–2003, 2004–2005, and 2005–2006. The observations from before 1992 show no S or L-mode fast ice in winter during 11 out of 60 years, but due to the poor spatial and temporal resolution it is not clear if these are years when no S or L-mode fast ice formed or whether the observations were made during a short break-up of an otherwise stable fast-ice cover.

This analysis is corroborated by the PSSM data from *Kern* [2008], for all the overlapping years except 1997. In 1997, the PSSM data show coastal polynyas within the fast ice area, but the AARI data show unbroken fast-ice during that period. In 1995 and 1996, the PSSM data also show coastal polynyas within the fast ice area, as well as a clear flaw polynya. The PSSM data for 1995, 1996, and 1997 should be interpreted such that the S-mode fast ice that formed in those years did break up and possibly reform during the January–April period. It is therefore clear that break-ups and reformations do occur in reality, even if they did not in 1997–1998. These appear to be limited to the formation phase, since there are no observed break-ups and reformations during the melting phase.

The modeled formation phase is therefore somewhat realistic, even if the model does not capture the 1997–1998 formation phase correctly. The modeled break-up is, however, only realistic when using the ellipse with $e = 1.3$. Further investigation indicates that a realistic break-up time can be simulated with the ellipse with nonzero isotropic tensile strength and the FMC, but only for a very narrow range of uniaxial compressive strength. Given that the observed break-up time only varies by about a month over the observed period one would expect the modeled break-up time not to be sensitive to errors in the forcing or the model parameters. The fact that correct break-up time is only modeled for a very narrow parameter range indicates that the modeled ice is not strong enough.

The most likely reason for the apparently too weak ice is that the ice growth rate in fall may be too small, causing the ice not to grow thick quickly enough during the freeze-up. This would explain the weak fast ice modeled in the formation phase, since the model is essentially tuned to reproduce fast-ice formation at the peak of the fast-ice season. If the fast ice becomes stable early then this also means that it will grow thicker than otherwise, since the dominant mode of advection is out of the fast-ice area. This would then cause a larger thickness difference between the ice within the fast-ice area and that outside it, making the simulation of erroneous polynyas (such as in Figure 8) less likely. The formation phase could therefore act as a preconditioning for the peak of the fast-ice season in such a way that a correctly simulated formation phase would make it more easy to tune the model to prevent the early break-up currently simulated in mid-May. Evaluation of the model with respect to thickness is, however, difficult since virtually no observations of the ice growth rate in the Severozemelsky region are publicly available. Recent advances in satellite remote sensing are likely to address this problem in the future. The ice growth rate can be increased by tuning the thermodynamic routines, but this was not attempted here.

The role of grounded pressure ridges has also been ignored here. It is clear that grounding does not play a leading role in fast-ice formation in the Kara Sea, but grounded pressure ridges may produce larger footers for the arches that form, effectively strengthening the arch structures. To test this I implemented the grounding scheme from *Lieser* [2004] and tested it with the FMC. This scheme simply assumes that ice that is thicker than one tenth of the local ocean depth is grounded and does not move. A small number of tests showed that using this grounding scheme the fast ice was more stable in the model, with reduced

frequency and size of the break-ups modeled during both formation and melt. This increased stability was, however, minor and not enough to prevent the large break-ups in January and mid-May. It is possible that more thorough exploration of the role of grounding would lead to a more stable fast ice in the model, but this initial investigation indicates that this is not likely.

Even though it suffers unrealistic break-ups the model does produce realistic fast-ice extent. To the author's best knowledge, this has not been achieved before in a realistic setting using a dynamic sea-ice model. The main reason fast ice forms the way it does in the Kara Sea is that the ice has sufficient uniaxial compressive strength in order to form arches between the Kara Sea islands. The model yield curve must therefore provide sufficient, and not too much uniaxial compressive strength in order to simulate this. In addition high maximum viscosity is needed and the momentum equation must be solved more accurately than is traditionally done. The solver presented in section 2.2 appears to be adequate for the current set-up, but the JFNK solver of *Lemieux et al*. [2010] may also be a feasible alternative.

6. Conclusions

This paper presents the first sea-ice model capable of producing land-fast ice in a realistic set-up based on internal model dynamics. The main assumption behind the approach taken here is that land-fast ice in the Kara Sea forms via static arching with the footers of the arches resting on a chain of islands offshore. The model itself is based on the well known viscous-plastic formulation first suggested by *Hibler* [1979], which is the basis for the vast majority of sea-ice models currently in use. The *Hibler* model was modified to use a more accurate solver for the momentum equation and a higher value for the maximum viscosity parameter than *Hibler* [1979] and most derivatives of that model. In addition it includes the modifications suggested by *König Beatty and Holland* [2010], which introduce tensile strength to the elliptic yield curve used by *Hibler* [1979], and a Coulombic yield curve (FMC), which also can possess tensile strength. The model suffers from unrealistic break-ups during the start and end of the fast ice season, but reproduces the fast ice extent and polynya formation well at the peak of the fast-ice season.

The necessary conditions for modeling land-fast ice with a viscous-plastic model are:

1. The yield curve used must provide the ice with sufficient uniaxial compressive strength, regardless of the yield curve shape. Here the range 15kPa$\lesssim\sigma_{uc}\lesssim$20 kPa was found to be appropriate (see Table 1).
2. The maximum viscosity of the viscous-plastic model must be larger than the conventional value of $\zeta_{max}=(2.5\times10^8\text{s})P$. In this study using at least $\zeta_{max}=(10^{13}\text{s})P$ was found to be necessary.
3. The momentum equation must be solved accurately. Here a residual error in the outer loop solver of $\epsilon_{OL}=10^{-4}$ m/s was found to be sufficient.

Appendix A: Uniaxial Compressive Strength

The uniaxial compressive strength for a given yield curve (σ_{uc}) is the value of σ_2 for which $\sigma_1=0$ for that particular curve. Note that $\sigma_1=\sigma_I+\sigma_{II}$ and $\sigma_2=\sigma_I-\sigma_{II}$.

In order to find σ_{uc} for the flexible Coulombic yield curve (FMC) we first solve the system of the two equations $\sigma_I=-\sigma_{II}$ and equation (10), replacing P with P^* to get the uniaxial tensile strength. This gives

$$\sigma_I'=-P^*k_T\sin\phi/(1-\sin\phi), \tag{A1}$$

which then gives

$$\sigma_{uc}=2\sigma_I' \tag{A2}$$

$$=-2P^*k_T\sin\phi/(1-\sin\phi) \tag{A3}$$

$$=\frac{-4p^*k_T\sin\phi}{(1-\sin\phi)(1-k_T+\sqrt{(1+\sin^2\phi)(1+k_T)^2})}, \tag{A4}$$

where the relationship between P^* and p^* comes from equations (8) and (16).

For the elliptic yield curve the relationship between σ_I and σ_{II} is an ellipse [*König Beatty and Holland*, 2010]:

$$\frac{(\sigma_I + P^*[1-k_T]/2)^2}{(P^*[1+k_T]/2)^2} + \frac{\sigma_{II}^2}{(P^*[1+k_T]/2e)^2} = 1. \tag{A5}$$

Insert $\sigma_I = -\sigma_{II}$ into the equation above to find σ_I' such that

$$\sigma_{uc} = 2\sigma_I' \tag{A6}$$

$$= -P^* \frac{1-k_T+\sqrt{(1-k_T)^2+4(1+e^2)k_T}}{1+e^2} \tag{A7}$$

$$= -2p^* \frac{1-k_T+\sqrt{(1-k_T)^2+4(1+e^2)k_T}}{(1+e^2)(1-k_T+\sqrt{(1+1/e^2)(1+k_T)^2})}. \tag{A8}$$

In both cases the uniaxial compressive stress calculated is negative, but in the text the uniaxial compressive strength reported is the absolute value of the stress.

Acknowledgments
The model development was financed by the DFG under HA 3166/2-1 "STARBUG." Forcing data for the model were provided by the National Center for Environmental Prediction (NCEP), the National Center for Atmospheric Research (NCAR), the University Corporation for Atmospheric Research (UCAR), the Alfred Wagner Institute in Bremen, Ocean Atmosphere Systems GmbH in Hamburg, the Global Runoff Data Centre in Koblenz, the Arctic and Antarctic Research Institute (AARI), and the Integrated Climate Data Center in Hamburg, as listed in section 2.1. Source code and input files are available from the author at request (einar.olason@nersc.no). I would like to thank Ingo Harms, Lars Kaleshke and Jan Backhaus for their help with this project. I would also like to thank Bruno Tremblay for nudging me in the right direction and his continued interest, Dirk Notz for his support and help in preparing this manuscript, and Jackie Richter-Menge for some pointers on the measurements of viscous creep. Finally, I would like to thank Bruno Tremblay, Jean-Francois Lemieux, and Dany Dumont for their review of the manuscript which helped greatly improve the final paper.

References

Arctic and Antarctic Research Institute (2007), *Sea Ice Charts of the Russian Arctic in Gridded Format, 1933-2006*, edited by V. Smolyanitsky et al., Natl. Snow and Ice Data Cent., Boulder, Colo., doi:10.7265/N5D21VHJ.

Backhaus, J. (2008), Improved representation of topographic effects by a vertical adaptive grid in vector-ocean-model (VOM). Part I: Generation of adaptive grids, *Ocean Modell.*, *22*(3–4), 114–127, doi:10.1016/j.ocemod.2008.02.003.

Bjornsson, H., A. J. Willmott, L. A. Mysak, and M. A. Morales Maqueda (2001), Polynyas in a high-resolution dynamic-thermodynamic sea ice model and their parameterization using flux models, *Tellus, Ser. A*, *53*, 245–265, doi:10.1034/j.1600-0870.2001.00113.x.

Bouillon, S., M. Á. Morales Maqueda, V. Legat, and T. Fichefet (2009), An elasticviscous-plastic sea ice model formulated on arakawa b and c grids, *Ocean Modell.*, *27*(34), 174–184, doi:10.1016/j.ocemod.2009.01.004.

Connolley, W. M., J. M. Gregory, E. Hunke, and A. J. McLaren (2004), On the consistent scaling of terms in the sea-ice dynamics equation, *J. Phys. Oceanogr.*, *34*(7), 1776–1780.

Divine, D. V., R. Korsnes, and A. P. Makshtas (2003), Variability and climate sensitivity of fast ice extent in the north-eastern Kara Sea, *Polar Res.*, *22*(1), 27–34, doi:10.1111/j.1751-8369.2003.tb00092.x.

Divine, D. V., R. Korsnes, and A. P. Makshtas (2004), Temporal and spatial variation of shore-fast ice in the Kara Sea, *Cont. Shelf Res.*, *24*(15), 1717–1736, doi:10.1016/j.csr.2004.05.010.

Divine, D. V., R. Korsnes, A. P. Makshtas, F. Godtliebsen, and H. Svendsen (2005), Atmospheric-driven state transfer of shore-fast ice in the northeastern Kara Sea, *J. Geophys. Res.*, *110*, C09013, doi:10.1029/2004JC002706.

Drescher, A., A. J. Waters, and C. A. Rhoades (1995), Arching in hoppers: I. arching theories and bulk material flow properties, *Powder Technol.*, *84*(2), 165–176, doi:10.1016/0032-5910(95)02981-7.

Dumont, D., Y. Gratton, and T. E. Arbetter (2009), Modeling the dynamics of the North Water polynya ice bridge, *J. Phys. Oceanogr.*, *39*(6), 1448–1461, doi:10.1175/2008JPO3965.1.

Feltham, D. L. (2008), Sea ice rheology, *Annu. Rev. Fluid Mech.*, *40*, 91–112, doi:10.1146/annurev.fluid.40.111406.102151.

Goldstein, R. V., N. N. Osipenko, and M. Leppäranta (2004), On the shape of the fast ice - drift ice contact zone, *Geophysica*, *40*(1–2), 3−13.

Haas, C., W. Dierking, T. Busche, and J. Hoelemann (2005), Envisat ASAR monitoring of polynya processes and sea ice production in the Laptev Sea, in *Proceedings of the 2004 Envisat & ERS Symposium (ESA SP-572)*, edited by H. Lacoste and L. Ouwehand, ESA Publications Division, Netherlands.

Hibler, W., J. Hutchings, and C. Ip (2006), Sea-ice arching and multiple flow states of Arctic pack ice, *Ann. Glaciol.*, *44*, 339–344, doi:10.3189/172756406781811448.

Hibler, W. D., III (1979), A dynamic thermodynamic sea ice model, *J. Phys. Oceanogr.*, *9*(4), 815–846, doi:10.1175/1520-0485(1979)009<0815:ADTSIM>2.0.CO;2.

Hibler, W. D., III, and E. M. Schulson (2000), On modeling the anisotropic failure and flow of flawed sea ice, *J. Geophys. Res.*, *105*(C7), 17,105–17,120, doi:10.1029/2000JC900045.

Hunewinkel, T., T. Markus, and G. Heygster (1998), Improved determination of the sea ice edge with SSM/I data for small-scale analyses, *IEEE Trans. Geosci. Remote Sens.*, *36*(5), 1795–1808, doi:10.1109/36.718647.

Ip, C. F., W. D. Hibler III, and G. M. Flato (1991), On the effect of rheology on seasonal sea-ice simulations, *Ann. Glaciol.*, *15*, 17–25.

Itkin, P., M. Losch, and R. Gerdes (2015), Landfast ice affects the stability of the arctic halocline: Evidence from a numerical model, *J. Geophys. Res. Oceans*, *120*, 2622–2635, doi:10.1002/2014JC010353.

Jenike, A. W. (1961), Gravity flow of bulk solids, *Bull. Utah Eng. Exp. Stn.*, *108*, 1–322.

Jenike, A. W. (1964), Steady gravity flow of frictional-cohesive solids in converging channels, *J. Appl. Mech.*, *31*, 5–11.

Kalnay, E., M. Kanamitsu, R. Kistler, W. Collins, D. Deaven, and L. Gandin (1996), The NCEP/NCAR 40-year reanalysis project, *Bull. Am. Meteorol. Soc.*, *77*(3), 437–471, doi:10.1175/1520-0477(1996)077¡0437:TNYRP¿2.0.CO;2.

Karcher, M., A. Beszczynska-Möller, F. Kauker, R. Gerdes, S. Heyen, B. Rudels, and U. Schauer (2011), Arctic ocean warming and its consequences for the Denmark Strait overflow, *J. Geophys. Res.*, *116*, C02037, doi:10.1029/2010JC006265.

Kern, S. (2008), Polynya area in the Kara Sea, Arctic, obtained with microwave radiometry for 1979-2003, *IEEE Trans. Geosci. Remote Sens.*, *5*(2), 171–175.

Kern, S., I. Harms, S. Bakan, and Y. Chen (2005), A comprehensive view of Kara Sea polynya dynamics, sea-ice compactness and export from model and remote sensing data, *Geophys. Res. Lett.*, *32*, L15501, doi:10.1029/2005GL023532.

König Beatty, C., and D. M. Holland (2010), Modeling landfast sea ice by adding tensile strength, *J. Phys. Oceanogr.*, *40*(1), 185–198, doi:10.1175/2009JPO4105.1.

Lammers, R., J. Pundsack, and A. Shiklomanov (2007), Variability in river temperature, discharge, and energy flux from the Russian pan-Arctic landmass, *J. Geophys. Res.*, *112*, G04S59, doi:10.1029/2006JG000370.

Lemieux, J.-F., and B. Tremblay (2009), Numerical convergence of viscous-plastic sea ice models, *J. Geophys. Res.*, *114*, C05009, doi:10.1029/2008JC005017.

Lemieux, J.-F., B. Tremblay, J. Sedláček, P. Tupper, S. Thomas, D. Huard, and J.-P. Auclair (2010), Improving the numerical convergence of viscous-plastic sea ice models with the Jacobian-free Newton-Krylov method, *J. Comput. Phys.*, *229*(8), 2840–2852, doi:10.1016/j.jcp.2009.12.011.

Lemieux, J.-F., L. B. Tremblay, F. Dupont, M. Plante, G. C. Smith, and D. Dumont (2015), A basal stress parameterization for modeling landfast ice, *J. Geophys. Res. Oceans*, *120*, 3157–3173, doi:10.1002/2014JC010678.

Lieser, J. L. (2004), A numerical model for short-term sea ice forecasting, PhD thesis, Univ. Bremen, Bremen, Germany.

Markus, T., and B. Burns (1995), A method to estimate subpixel-scale coastal polynyas with satellite passive microwave data, *J. Geophys. Res.*, *100*(C3), 4473–4487, doi:10.1029/94JC02278.

Matchett, A. J. (2007), The shape of the cohesive arch in hoppers and silos some theoretical considerations, *Powder Technol.*, *171*(3), 133–145, doi:10.1016/j.powtec.2006.10.010.

Richter-Menge, J. A., and G. F. N. Cox (1995), The creep of saline ice at low stresses and high temperatures, paper presented at the 5th International Offshore and Polar Engineering Conference, International Society of Offshore and Polar Engineers, Hague, Netherlands.

Selyuzhenok, V., T. Krumpen, A. Mahoney, M. Janout, and R. Gerdes (2015), Seasonal and interannual variability of fast ice extent in the southeastern laptev sea between 1999 and 2013, *J. Geophys. Res. Oceans*, *120*, 7791–7806, doi:10.1002/2015JC011135.

Semtner, A. J. (1976), Model for thermodynamic growth of sea ice in numerical investigations of climate, *J. Phys. Oceanogr.*, *6*(3), 379–389, doi:10.1175/1520-0485(1976)006¡0379:AMFTTG¿2.0.CO;2.

Timco, G. W., and W. F. Weeks (2010), A review of the engineering properties of sea ice, *Cold Reg. Sci. Technol.*, *60*(2), 107–129, doi:10.1016/j.coldregions.2009.10.003.

Tremblay, L.-B., and M. Hakakian (2006), Estimating the sea ice compressive strength from satellite-derived sea ice drift and NCEP reanalysis data, *J. Phys. Oceanogr.*, *36*(11), 2165–2172, doi:10.1175/JPO2954.1.

Tremblay, L.-B., and L. A. Mysak (1997), Modeling sea ice as a granular material, including the dilatancy effect, *J. Phys. Oceanogr.*, *27*(11), 2342–2360, doi:10.1175/1520-0485(1997)027¡2342:MSIAAG¿2.0.CO;2.

Volkov, V. A., O. M. Johannessen, V. E. Borodachev, G. N. Voinov, L. H. Pettersson, L. P. Bobylev, and A. V. Kouraev (2002), *Polar Seas Oceanography: An Integrated Case Study of the Kara Sea*, Springer, London, U. K.

Wang, K. (2007), Observing the yield curve of compacted pack ice, *J. Geophys. Res.*, *112*, C05015, doi:10.1029/2006JC003610.

Weiss, J., H. L. Stern, and E. M. Schulson (2007), Sea ice rheology from in-situ, satellite and laboratory observations: Fracture and friction, *Earth Planet. Sci. Lett.*, *255*(1-2), 1–8.

Zhang, J., and W. D. Hibler, III (1997), On an efficient method for modeling sea ice dynamics, *J. Geophys. Res.*, *102*(C4), 8691–8702, doi:10.1029/96JC03744.

Zyryanov, D. V., and R. Korsnes (2003), A numerical model for simulation of sea ice destruction due to external stress in geoscale areas, in *Proceedings of the 1st International PFC Symposium on Numerical Modeling in Micromechanics via Particle Methods*, edited by H. Konietzky, pp. 29–36, A. A. Balkema, Gelsenkirchen, Germany.